

Role of high-temperature Equal-Channel Angular Pressing strain path on secondary-phase precipitation in a T6-Al-Cu-Li-Mg-Ag-Zr-Sc alloy

M. Cabibbo, S. Acierno, C. Paoletti

Equal-channel angular pressing (ECAP) is known to induce significant grain refinement and formation of tangled dislocations within the grains. These are induced to evolve to form low-angle boundaries (i.e., cell boundaries) and eventually high-angle boundaries (i.e., grain boundaries). On the other hand, precipitation sequence of age hardening aluminum alloys can be significantly affected by pre-straining, and severe plastic deformation. Thus, ECAP is expected to influence the T6 response of aluminum alloys. In this study, a complex Al-Cu-Mg-Li-Ag-Zr-Sc alloy was subjected to ECAP following different straining paths. The alloy was ECAP at 460K via route A, C, and by forward-backward route A up to 4 passes. The alloy was also aged at 460K for different durations after ECAP. It resulted that T_1 - Al_2CuLi phase was the one that mostly showed a precipitation sequence speed up induced by the tangled dislocations formed during ECAP. The T_1 phase was found to grow with aging time according to Lifshitz-Slyozov-Wagner power-low regime.

KEYWORDS: ECAP, Al-Cu-Mg-Li-Ag-Zr-Sc ALLOY, SECONDARY-PHASE PRECIPITATION, TEM

INTRODUCTION

Al-Cu-Li based alloys are recognized as important metallic materials for structural applications requiring a combination of high strength, low density, high fracture toughness and good corrosion resistance [1-6]. All these mechanical and physical characteristics are indeed particularly relevant for aerospace applications [1-3]. Moreover, weight reduction is now widely considered as a primary means to lower fuel cost in the aeronautics and aerospace industry [3]. A reduction in aircraft weight reduces fuel consumption, thus increasing the payload capability [4]. Accordingly, lithium, as the lightest metal known, was used as additional element in a number of aluminum series alloys. An addition of 1 wt.% Li reduces the Al density by 3%, and usually increases the alloy elastic modulus by some 6% [7].

In the last three decades scientific research on Al-Li-based alloys mostly focused on Al-Cu-Li, Al-Cu-Mg, and Al-Mg-Li alloys [10-13]. In the base Al-Cu-Li system, the two secondary phase precipitates that are induced to form belong to the binary Al-Cu, Al-Li, and ternary Al-Cu-Li systems. Thus, the precipitating phases are GP-I, GP-II zones, θ'' , θ' phase, to end at the stable θ (Al_2Cu), and similar formation process of θ' to θ (Al_3Li), and T_1 (Al_2CuLi) phase [14].

Marcello Cabibbo, Chiara Paoletti

DIISM / Università Politecnica delle Marche, Ancona -
corresponding author (Marcello Cabibbo):
e-mail m.cabibbo@staff.univpm.it; Tel. 0712204728.

Stefano Acierno

Dipartimento di Ingegneria, Università degli studi del Sannio,
Benevento

Addition of other alloying elements (especially Mg, Mn, Ag, Zn, Zr) results in a wider variety of precipitating secondary-phases. Addition of such elements promotes complex precipitation sequences that also depend on processing and aging conditions. Thus, the Al-Cu-Li-X alloy systems are known to be age-hardened through different secondary-phases, such those with Mg, S', and S (Al_2CuMg), T' ($(Al,Zn)_{49}Mg_{32}$), the one with Zr, β' (Al_3Zr), and the Li-containing σ ($Al_5Cu_6Li_2$), which actually form at high ageing temperatures. When this phase forms, it shows its maximum strengthening potentials for size range of 30-50 nm. Both T' ($(Al,Zn)_{49}Mg_{32}$) and β' (Al_3Zr), are dispersoids that typically lies along grain boundaries.

As for the role of Ag, in the complex Al-Cu-Li-X alloy, it was widely documented that it tends to segregate in the T_1 - Al_2CuLi phase, and in the S'- Al_2CuMg phase, thus contributing to their microstructure strengthening effects [15,16].

Together with the above-mentioned strengthening fine-dispersed precipitation phases, the lithium-containing aluminum alloys are engineered in terms of ductility. With this respect, the refining processes of both grains and cells are important microstructure features for improving the alloy mechanical properties. Thence, alloying elements, heat treatments and plastic deformation are the three major means to tailoring a sound and technological interesting Li-bearing complex aluminum alloy [17].

The AA2198 (Al-Cu-Li-Mg-Ag-Zr), and similar alloys, sometimes referred as Weldalite® alloys, are known to be characterized by the formation of all the above-mentioned secondary-phases that are induced to precipitate under annealing and peak ageing.

It is well known that pre-strain, or even plastic deformation techniques applied before or after annealing and aging to peak hardness is able to influence the whole secondary-phase precipitation sequences in aluminum alloys [18,19]. With this respect, severe plastic deformation techniques applied to aluminum alloys was reported to significantly modify the alloy response to T6 temper. Thus, more specifically, due to the variety of hardening phases induced by the T6 treatments in Al-Cu-Mg-Li-X alloys, SPD are likely to significantly change the precipitation kinetics of most, if not all, the secondary phases [14]. Among the different SPD techniques, the equal-channel angular pressing (ECAP) is surely one of the most important cost-effective such technique [20,21]. During ECAP the material is forced to plastically deform by shearing at the intersection of the angular channels. The sample retains the same cross-sectional area after pressing, so that it is possible to repeat the pressing several times.

With this respect, previous works by this author showed that the different strain paths to which tempered aluminum alloys can be subjected by ECAP are able to effectively influence the secondary-phase precipitates volume fraction [22,23]. In ECAP, samples are usually in form of cylindrical or square-section rod billets that are continuously forced to follow a linear path into a L-shaped equal-channel [24,25]. Strain paths in ECAP correspond to different processing routes [26,27]. Among these, here routes A and route C were taken into consideration. Route A involves no specimen rotation between consecutive ECAP passes, while by route C the billet is continuously rotated by 180° between passes. In addition, an evolution of the ECAP process included a further different pathway, consisting on reversing the billet path direction between consecutive passes. This is called a forward-backward ECAP (FB-ECAP) process [26-28]. In particular, a forward-backward cycling shear deformation by ECAP or similar techniques was shown to induce ultrafine-grained aluminum alloys in a more effective way [27,28]. This would mean that the shear deformation path in FB-ECAP is potentially able to refine the aluminum microstructure with lesser passages into the die. It is thus expected that the recombination of tangled dislocations to form cell boundaries, and in turn, the cell boundary evolution to grain boundary, is likely to be faster in FB-ECAP respect to conventional ECAP shear paths.

In the present work, a Sc-added Al-Cu-Li-Mg-Ag-Zr alloy was subjected to ECAP with different strain paths (i.e., routes and modes). More specifically, billets were processed up to 4 passes by route A, C, and by FB-ECAP route A. These two routes and different processing modes introduced tangle dislocations (TDs), cell (low-angle boundaries, LABs), and grain (high-angle boundaries, HABs) at different crystallographic planes. It was thus possible to determine the role of the specific shear strains to which the alloy was subjected on the precipitation kinetics of the alloy hardening secondary-phase precipitates.

EXPERIMENTAL DETAILS AND METHOD

The studied alloy has a composition (wt.%) of Al-3.0Cu-1.0Li-0.4Mg-0.4Ag-0.2Zr-0.5Sc, which is a Sc-modified Weldalite® alloy. Cylindrical billets of 9.8 mm in diameter and 100 mm long were machined from extruded bars. The billets were then solution treated in an air standard convection furnace at 815K for 4 h, followed by water quenching. To determine the aging hardness peak, the alloy was aged at 460K for duration ranging 10-to-2880 min (10 min to 2 days).

ECAP was performed on annealed billet at the same aging temperatures of 460K. An open die, consisted of a block of SK3 tool steel (Fe-1.1%C) and fastened with steel bolts, was used. ECAP was carried out under uniaxial pressing forces ranged between 40–80 kN and a pressing speed of 100 mm/min. The ECAP L-shaped channel had a circular cross-section diameter of 10 mm, consisting of two linear parts intersecting at an angle $\Phi = 90^\circ$ with a curvature extending over an angle $\Psi = 20^\circ$. Based on this two-channels geometry, a cumulative shear strain $\epsilon_{eq} = 1.08$ was imposed to the billet at each pass [21,25]. Microstructure inspections and microhardness tests were performed along the ECAP y-plane by cutting slices of the billet as to make measurements at the center zone of the billet. This plane is the one containing the extruded and the plastic shear directions, as depicted in Figure 1. ECAP route A does not involve any billet rotation between passes, route C consists of rotating the billet by $+90^\circ$ at each consecutive passage into the die, and the variant forward-backward consists of inverting the billet head at each ECAP pass during route C. Microstructure inspections were carried out after ECAP-A/4, ECAP-C/4, and FB-ECAP-A/4. Inspections were carried out both after ECAP and after ECAP followed by aging at 460K. In this latter case, the inspections were carried out at the T6 alloy metallurgical state, and at the annealing time to reach the hardness peak after, respectively, ECAP-A/4, ECAP-C/4, and FB-ECAP-A/4. TEM samples were ground and polished to $\sim 150 \mu\text{m}$, punched into discs of 3mm diameter, and then electropolished

by a Gatan™ Tenupol-5® working at 12V and using a solution of 1/3 nitric acid in methanol at $T = -35^\circ\text{C}$.

TEM discs were examined in a Philips™ CM20® operated at 200 kV, using a double-tilt specimen holder equipped with liquid nitrogen cooling stage. Secondary-phases precipitates were identified by using selected area electron diffraction (SAED). Thin foil thickness, t , was measured on TEM by diffracted beam intensity variation under dual beam conditions, using converged electron beam diffraction (CBED) patterns. Tangled dislocation (TD) density, ρ_{TD} , was calculated through the count of interception points between the mesh and the existing dislocations, n_{disl} in the TEM micrographs. This was evaluated by $\rho_{TD} = 2n_{disl}/(l_{mesh}t_{TEM})$, where, l_{mesh} is the total length of the mesh, and t_{TEM} is the thickness of the TEM foil. Cell (LAB) and grain boundary (HAB) misorientation were measured by Kikuchi band patterns. The misorientation angle measurement procedure by Kikuchi pattern on TEM is fully described elsewhere in a previous published work by this author [24,25,29,30]. TEM quantitative analyses of secondary phase precipitates were carried out on crystallographic Al_{002} , Al_{111} , and on Al_{210} planes, depending on the habit plane of the different existing phase; tangled dislocation density was measured along the crystallographic Al_{002} planes.

All the statistical evaluations were carried out according to conventional stereology methods [31] with the help of Image pro-plus® analysis software.

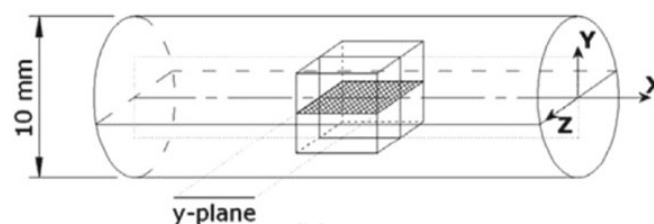


Fig.1 - Characteristic deformation directions in ECAP billet. The y-plane contains the shear deformation bands induced by ECAP and it is the one selected for TEM inspections. ECAP direction is along the billet X direction.

Polarized optical microscopy was carried out by surface polishing and electro-chemical etching at room temperature using a solution of 4% HBF_4 in methanol at 20 V for few seconds.

A Remet™ HX-1000® microhardness tester was used to

carry out at least 12 measurements per each experimental condition. To determine the curve peak, hardness was measured on the ECAP y-plane surfaces after ECAP-A/4, ECAP-C/4, and FB-ECAP-A/4, and after post-ECAP aging at 460K for times ranging 10 to 2880 min (2 days).

RESULTS AND DISCUSSION

T6 temper microstructure

The T6-hardening treatment consisted of annealing at 813K/4h, water quenching, and aging at 460K for time, t , of 10, 20, 30, 60, 90 min, 2, 4, 6, 8, 10, 16 h, 1, and 2 days. Figure 2a shows the T6 hardness, H , vs. aging time. It resulted a marked hardness peak at 460K/6h. This T6-peak condition corresponded to the formation of different nanometric precipitates, such GP zones, T_1 -(Al₂CuLi), δ' -(Al₃Li), and θ''/θ' -(Al₂Cu) precipitates. Boundary pinning β -(Al₃Zr) dispersoids also characterized the T6 alloy microstructure. These hard-

ening secondary-phase precipitates were observed by TEM inspections and Figure 2b and 2c shows representative BF-TEM micrographs. In particular, Figure 2b and 2c are TEM micrographs showing the Al₁₁₁ and Al₀₀₂ planes, respectively. On Al₀₀₂ plane (Figure 2b) GP zones, nanometric θ' disc and δ' spherical precipitates were found within the grains. Grain boundaries were decorated with larger rounded β' -Al₃(Zr,Sc) dispersoids. On Al₂₁₀ plane (Figure 2d) GP zones and few θ'' disc precipitates were detected.

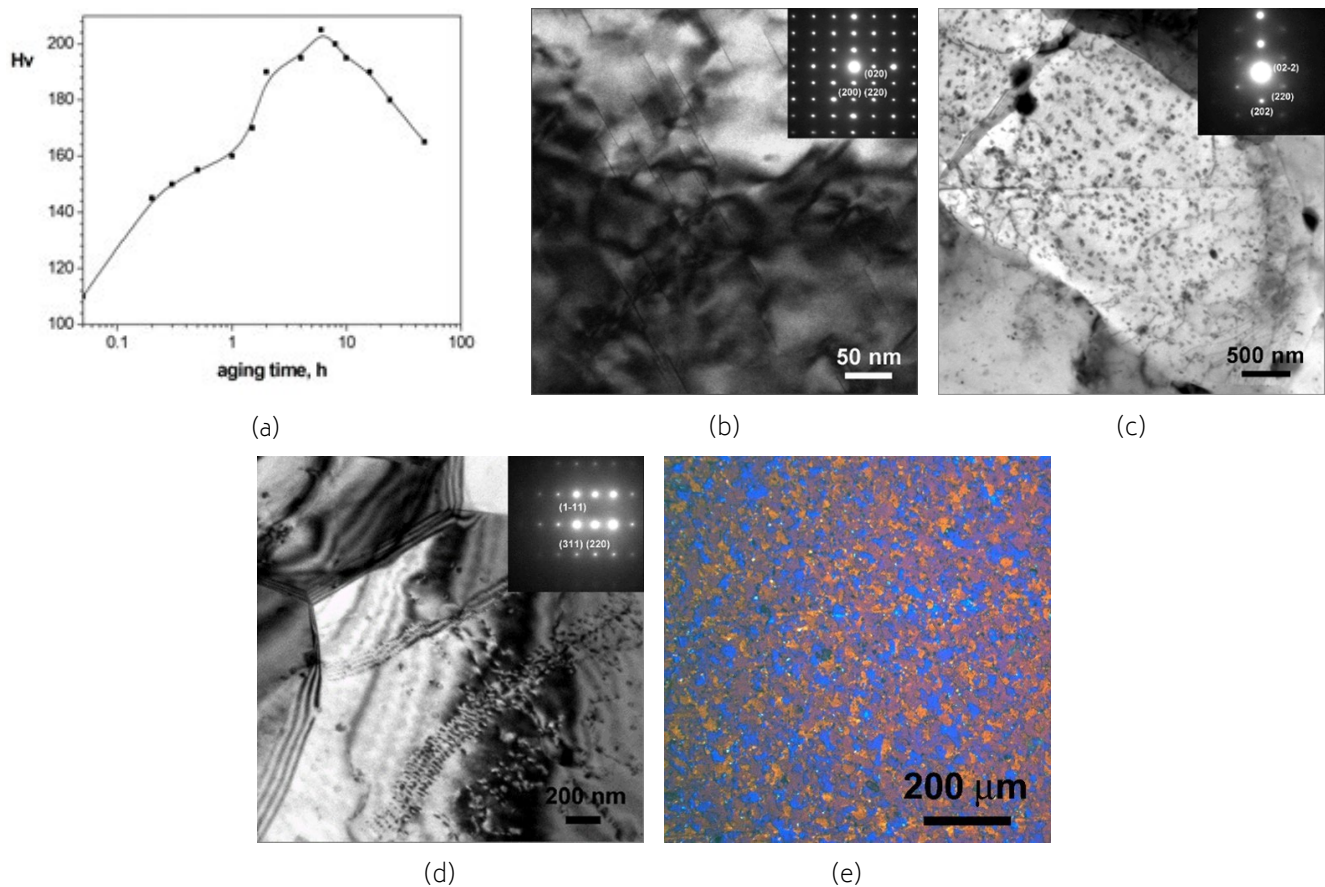


Fig.2 - Hardness, H , vs. aging time, t , of the alloy annealing at 813K/4h and aging at 460K, a), BF-TEM showing the microstructure at T6 hardness peak condition (aging at 460K/6h), Al₀₀₂, b), Al₁₁₁, c), and Al₂₁₀ crystallographic plane, d). Polarized optical micrograph showing the alloy T6 grained structure, e).

T6 treatment showed a significant mean grain size reduction, from the as-received $D_g = 36 \pm 3 \mu\text{m}$, down to $D_g = 24 \pm 2 \mu\text{m}$, with an aspect ratio of 0.94, that is, with equiaxed grained structure (Figure 2e). This means that a size reduction of almost 30 % was induced upon annealing at 715K/4h. This is essentially due to the presence of the Sc- and Zr-dispersoids that effectively pinned the grain boundary coar-

sening tendency during annealing. In fact, it is well known that Sc and Zr form thermally stable β' -Al₃(Sc,Zr) spherical dispersoids that effectively pin the grain and cell boundaries [32,33]. In particular, in [32] it was reported that Sc diffusion becomes significant from 523K, and that the Al₃(Sc_{1-x}Zr_x) dispersoid formation is controlled by Sc diffusion below 623K, where Zr diffusion becomes effective. Thence, at the

annealing temperature of 813K $\text{Al}_3(\text{Sc}_{1-x}\text{Zr}_x)$ dispersoids are formed to remain stable upon further aging. The effectiveness of the grain, cell boundary and dislocation pinning effect exerted by the nanometric size $\text{Al}_3(\text{Sc}_{1-x}\text{Zr}_x)$ dispersoids not only comes from their stability at the aging temperatures

but it also originates from their crystallographic coherency with the Al-matrix. This latter aspect is documented in Figure 3, where Ashby-Brown strain contrast characterizes the showed $\beta\text{-Al}_3(\text{Sc}_{1-x}\text{Zr}_x)$ dispersoids.

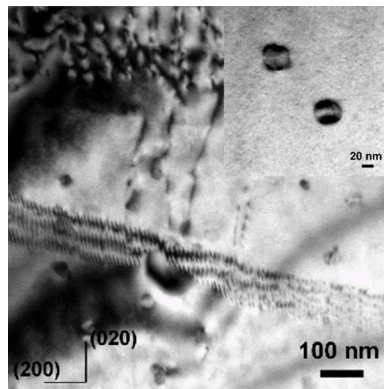


Fig.3 - $\text{Al}_3(\text{Sc}_{1-x}\text{Zr}_x)$ dispersoids showing Ashby-Brown strain contrast in the alloy tempered at 714K/4h + aging at 460K/6h. Inset is a detail of two β' dispersoids showing Ashby-Brown contrast.

Microstructure after ECAP

ECAP was carried out at 460K by three different routes: route A (no rotation between passes), route C (180° rotation between passes), and forward-backward pressing (FB-ECAP) following route A. In all the three modes, the billets were pressed four times into the ECAP die (respectively, ECAP-A/4, ECAP-C/4, and FB-ECAP-A/4). The alloy was ECAP after annealing at 813K/4h and water quenching to room temperature. The main purpose for comparing the three SPD ECAP shearing modes was to correlate the specific shear path and deformation to the induced different Al-Cu-Li-Mg-Ag-Zr-Sc alloy secondary-phase precipitates evolution. In fact, it is well known that during ECAP the alloy is subjected to a thermo-mechanical stress in terms of both shear bands that run at a typical angle of 40-42° respect to the exit direction (x direction in Figure 1) [21], and adiabatic heating [25].

TEM inspections showed a significant influence of the ECAP shear deformation on the secondary-phase precipitation kinetics. In particular, ECAP was able to multiply the sites of GP zone agglomeration and secondary phase precipitation through tangled dislocations and cell boundary formation. Figure 4 reports representative TEM micrographs of the

ECAP-A/4, ECAP-C/4, and FB-ECAP-A/4 conditions. The figure clearly shows that the tangled dislocations act as preferential sites of GP and secondary-phase formation.

Evaluation of the tangled dislocation density in the three experimental cases allowed correlating them with the ECAP-induced GP and secondary-phase precipitation. It resulted that the tangled dislocation density, $\rho_{\text{disl}'}$ was the highest in the FB-ECAP-A/4, a little lower in the ECAP-A/4, and the lowest in ECAP-C/4 (Table 1). That is, the following hierarchy of tangled dislocation density can be drawn: FB-ECAP-A/4 > ECAP-A/4 > ECAP-C/4. The highest dislocation density corresponded to the highest amount of GP agglomeration along the dislocation line defects and to a clear initiation of secondary-phase formation sequence. GP zones were found to form preferentially along the free dislocations within the grains, and early precipitation stages of secondary-phase precipitation started to occur (Figure 4b-to-f).

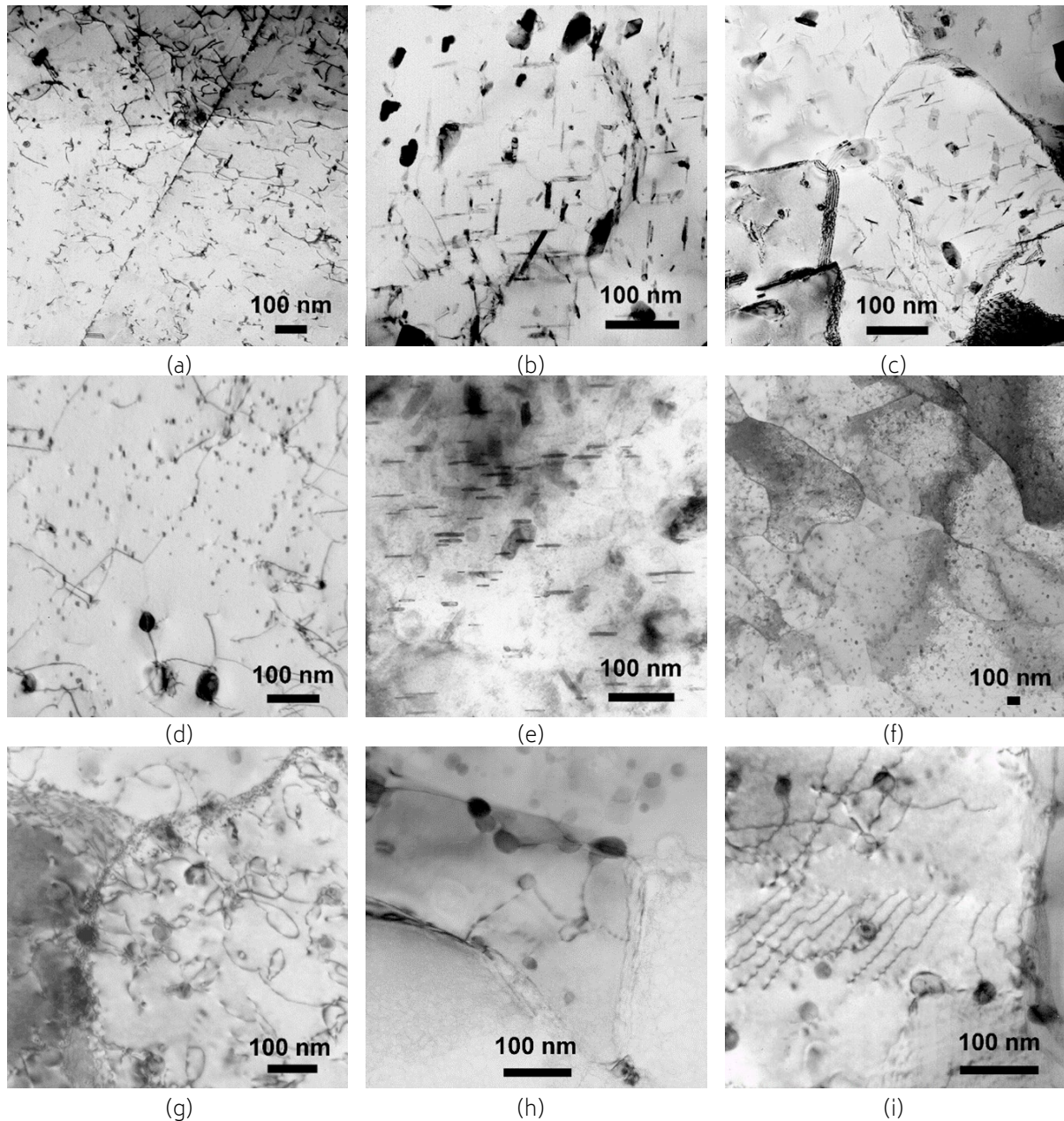


Fig.4 -BF-TEM of ECAP-A/4 where the crystal is oriented as to show Al_{100}' , a), Al_{110}' , b), Al_{111}' plane, c); ECAP-C/4 along Al_{100}' , d), Al_{110}' , e), Al_{111}' , f); and FB-ECAP-A/4 along Al_{100}' , g), Al_{110}' , h), Al_{111}' , i). Al-Cu clusters and GP zones were detected along the three planes; θ' - Al_2Cu were detected aligned along Al_{100}' ; T_1 - Al_2CuLi along Al_{110}' ; δ - Al_3Li along Al_{111}' .

These are: θ' at Al_{100} plane, T_1 at the Al_{110} plane, and δ at Al_{111} plane. Thence, the shear deformation during ECAP at 460K, the added adiabatic heating to which the alloy was subjected during the four passes, were responsible for the formation of GP zones and initial precipitation sequence along tangled dislocations of θ' , T_1 , and δ secondary-phases.

On the other hand, it is well known that ECAP is able to significantly refine the grained structure of aluminum already at the early stages of plastic deformation. In the present case, the mean grain size, after all the three ECAP routes was measured by a statistical meaningful number of individual measuremen-

ts. These were at least 250 per each condition and the identification of grain and cell structures was carried out by means of Kikuchi band analyses. This is fully described elsewhere in previously published works by the present author ([25,29,30] and references therein). A grain was identified as a portion of the crystal all-around surrounded by high-angle boundaries (HABs). On the other hand, a cell was identified as a matrix portion surrounded by at least one low-angle boundary (LAB) line. Figure 5 reports representative low-magnification BF-TEM micrographs showing the refined grained structure after ECAP-A/4, ECAP-C/4, and FB-ECAP-A/4. As reported

in Table 1, mean grain size was significantly reduced to 1-to-3 μm depending on the ECAP route. That is, the strongest grain size reduction was obtained after ECAP-C/4, being the ECAP-A/4 the one with the coarser refined grained structure. Thus, the following hierarchy of grain size reduction can be drawn: ECAP-C/4 > ECAP-A/4 > FB-ECAP-A/4. This means that the ECAP-C/4 resulted to be the most effective path for

grain size reduction, with minimal dislocation dispersion to form tangled dislocations, rather than cell boundaries. These latter were lower in density in ECAP-A/4 microstructure since most of them contributed to form both cell and grain boundaries. This finding well agrees with other previously published results [19-21] and with results reported by the present author elsewhere in other aluminum alloys [24,25].

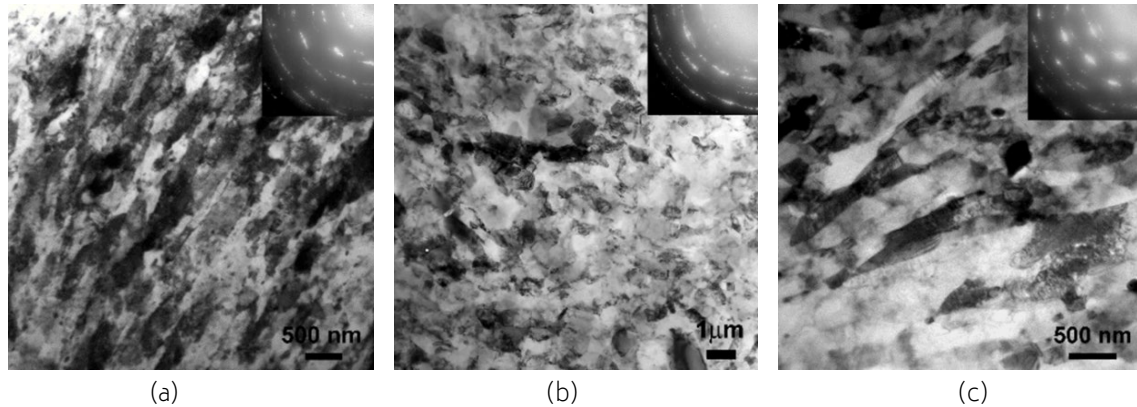


Fig.5 -LM BF-TEM showing the alloy grain structure along Al110 after ECAP-A/4, a), ECAP-C/4, b), and FB-ECAP-A/4, c). Insets are SAEDPs showing the process of grain refinement through formation of concentric diffraction rings.

The Al-Cu-Mg-Li-Ag-Zr-Sc alloy was subjected to ECAP at 460K by same routes and by post-ECAP aging at same T6 conditions as obtained by the plot of Figure 2a (460K/6h). Figure 6 shows the microstructure after post-ECAP aging at 460K/6h, and in all the three SPD routes a certain amount of secondary-phase coarsening respect to the case of the undeformed T6-tempered alloy was observed (see Figure 2b-d). In particular, quite few traces of GP zones are visible. All the agglomerations and element clustering grew up to eventually precipitate as nanometric secondary-phases. Thus, the alloy microstructure was mostly characterized by the co-presence

of small (few nanometric in size) to coarser (few tens of nanometer in size) secondary-phase precipitates. These were identified by SAEDPs as T_1 - Al_2CuLi , Ω - $\text{Al}_x(\text{CuLi})_y$ -type, θ'' - Al_2Cu , and S' - Al_2CuMg . That is, the microstructure of all the three ECAP path conditions is similar to an overaged metallurgical condition rather than a T6 hardness peak one. Thus, these microstructure findings confirmed that both tangled dislocation and, to some extent cell boundaries, contributed to accelerate the precipitation sequences of most of the detected secondary-phase precipitates.

Tab.1 - Tangled dislocation density, ρ_{disl} , cell, D_{cell} , and grain, D_g , size, after ECAP-A/4, ECAP-C/4, and FB-ECAP-A/4 at 460K. Measured mean number density of GP zones and precipitates, n_v , of all detected secondary-phases T_1 , θ , δ induced to form under ECAP-A/4, ECAP-C/4, and FB-ECAP-A/4 at 460K. Mean longer-edge lengths of the T_1 platelets, l_{T_1} , at alloy T6-condition and after ECAP at 460K are also reported.

	annealed 813K/4h + aged 460K/6h	ECAP-A/4 at 460K	ECAP-C/4 at 460K	FB-ECAP-A/4 at 460K
$\rho_{\text{disl}}, 10^{14}\text{m}^{-2}$	0.18 ± 0.06	2.5 ± 0.4	1.5 ± 0.5	2.9 ± 0.5
$D_{\text{cell}}, \text{nm}$	-	250 ± 40	540 ± 40	180 ± 40
$D_g, \mu\text{m}$	24 ± 2	1.4 ± 0.2	1.7 ± 0.3	1.6 ± 0.4
$n_v(\text{GP}+T_1), \mu\text{m}^{-3}$	330 ± 3	60 ± 10	40 ± 5	70 ± 10
$n_v(\text{GP}+\theta), \mu\text{m}^{-3}$	90 ± 2	16 ± 4	12 ± 3	18 ± 4
$n_v(\text{GP}+\delta), \mu\text{m}^{-3}$	190 ± 2	20 ± 4	14 ± 3	32 ± 4
l_{T_1}, nm	70 ± 10	45 ± 5	50 ± 5	40 ± 5

During post-ECAP aging, two other secondary-phase precipitates formed, Ω and S' . These two phases were detected to form at same crystallographic planes of, respectively, T_1 and δ' .

Table 2 shows the statistical data of all the detected secondary-phase precipitates induced to form during ECAP at 460K followed by aging at 460K/6h (T8 temper). As already documented by Figure 6, the overaged T8 ECAP + aging at

460K/6h conditions favoured the formation of Ω and S' phases. These two phases were not reported to form upon alloy T6 condition (Figure 2).

The Table does not include the $\beta\text{-Al}_3(\text{Sc}_{1-x}\text{Zr}_x)$ dispersoids as they are thermally stable at the post-ECAP aging temperatures and they act as grain boundary-pin elements, rather than phase-hardening.

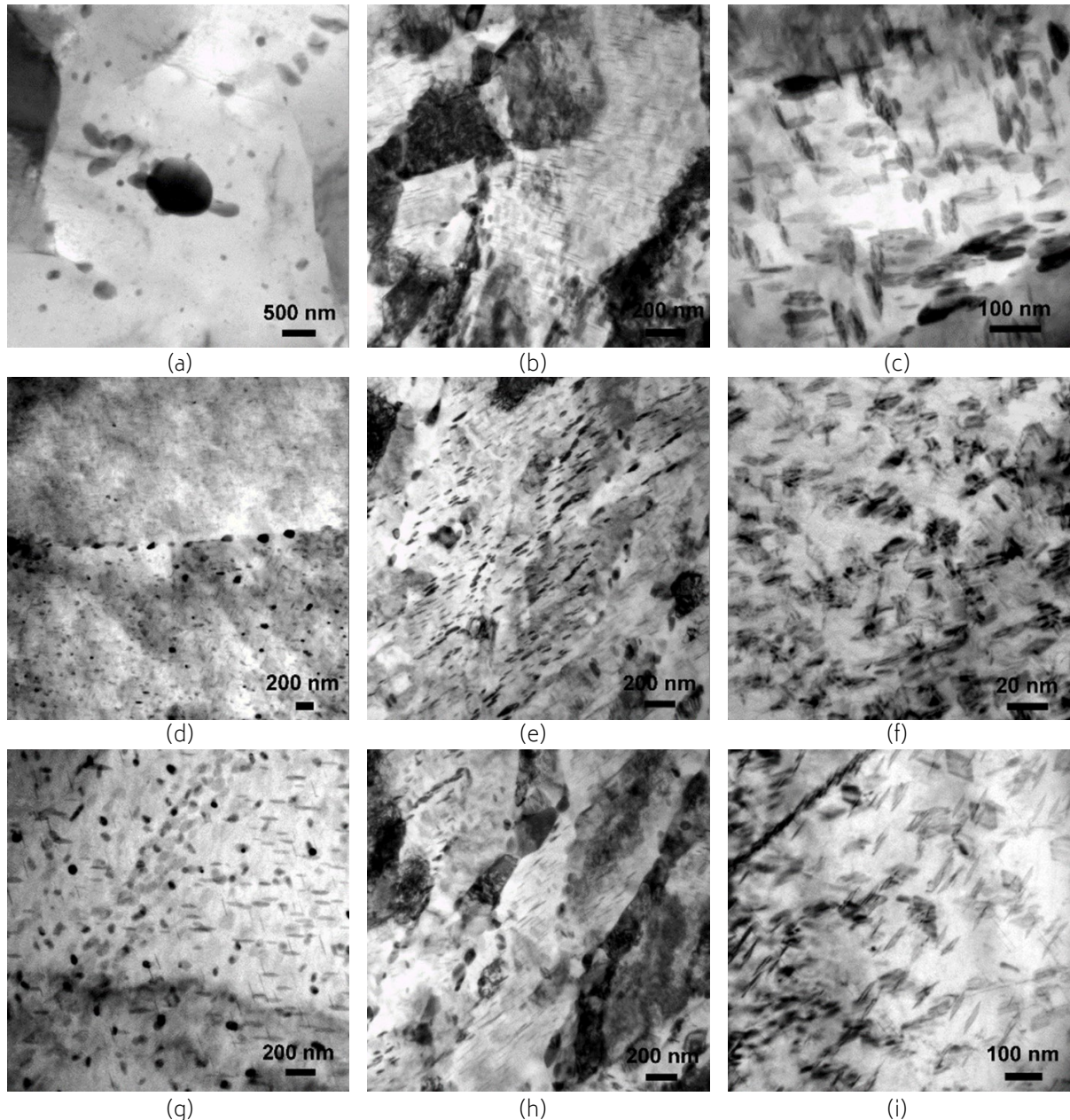


Fig.6 -Microstructures of the post-ECAP 460K/6h annealed alloys showing the different secondary-phase precipitates. BF-TEM of ECAP-A/4 along Al_{100} , a), Al_{110} , b), and Al_{111} plane, c); ECAP-C/4 along Al_{100} plane, d), Al_{110} , e), and Al_{111} , f); FB-ECAP-A/4 along Al_{100} plane, g), Al_{110} , h), and Al_{111} , i).

Tab.2 - Tangled dislocation density, ρ_{disl} , cell, D_{cell} , and grain, D_g , size, secondary-phase precipitate mean number density, $n_v(T_1)$, $n_v(\Omega)$, $n_v(\theta)$, $n_v(\delta)$, $n_v(S)$, and size, d_{T_1} , d_Ω , d_θ , d_δ , d_S formed after ECAP-A/4, ECAP-C/4, and FB-ECAP-A/4 and subsequent aging at 460K/6h (overaged T8 condition). Mean longer-edge length of the T_1 platelets, l_{T_1} , is also reported.

	ECAP-A/4 +aged at 460K/6h	ECAP-C/4 +aged at 460K/6h	FB-ECAP-A/4 +aged at 460K/6h
ρ_{disl} , 10^{14}m^{-2}	1.9 ± 0.5	0.9 ± 0.3	1.6 ± 0.3
D_{cell} , nm	320 ± 40	710 ± 40	290 ± 40
D_g , μm	1.8 ± 0.3	1.9 ± 0.3	2.0 ± 0.3
$n_v(T_1)$, μm^{-3}	250 ± 20	210 ± 20	280 ± 20
$n_v(\Omega)$, μm^{-3}	210 ± 20	210 ± 20	250 ± 20
$n_v(\theta)$, μm^{-3}	105 ± 5	110 ± 5	110 ± 10
$n_v(\delta)$, μm^{-3}	210 ± 10	190 ± 10	220 ± 20
$n_v(S)$, μm^{-3}	50 ± 10	40 ± 10	50 ± 10
d_{T_1} , nm	60 ± 5	55 ± 5	70 ± 5
d_Ω , nm	65 ± 5	50 ± 5	70 ± 5
d_θ , nm	35 ± 5	45 ± 5	35 ± 5
d_δ , nm	30 ± 5	28 ± 5	34 ± 5
d_S , nm	35 ± 5	30 ± 5	35 ± 5
l_{T_1} , nm	145 ± 10	155 ± 10	130 ± 10

The T8 metallurgical condition induced a number density rise, $n_v(T_1)$ and $n_v(\Omega)$, from ECAP-C/4 to ECAP-A/4 and to FB-ECAP-A/4. This means that the shear path influenced the precipitation of the T_1 and Ω phases. The other strengthening phases did not change their number fraction with different ECAP routes. The size of all the secondary-phase precipitates was not affected by the specific ECAP shear path as they did not change from ECAP-A/4, ECAP-C/4, and FB-ECAP-A/4. On the other hand, the tangled dislocation density, ρ_{disl} , almost double in the FB-ECAP-A/4, and ECAP-A/4, respect to the ECAP-C/4 condition. In particular, FB-ECAP-A/4 reported tangled dislocation density quite close to the one measured in the ECAP-A/4 and thus the shear deformation process seemed to induce a similar dislocation rearrangement during ECAP passes through these two processing routes.

On the other hand, also the cell and grain structure appeared to be quite similar, contributing to confirm the microstructure evolution similarities between ECAP-A/4 and

FB-ECAP-A/4. On the contrary, the lower dislocation density measured in the ECAP-C/4 is most likely due to the dislocation crystallographic recombination phenomenon induced during the 180° billet rotation between ECAP passes. Accordingly, as well-documented in hundreds of research contributions so far ([55-79], and references therein) the grain refining efficiency differences between namely route A and route C is particularly sensitive to the ECAP shear path. Thence, FB-ECAP-A/4 and ECAP-A/4 resulted to be more grain size refining-effective than ECAP-C/4.

Microhardness

Micro-hardness, H , was measured along the y -plane of the three ECAP-A/4, ECAP-C/4, and FB-ECAP-A/4 conditions after ECAP and after subsequent aging at 460K for the same times selected to determine the T6 temper hardness peak of the un-deformed alloy (Figure 2a). The plots of H vs. aging time of the ECAP-A/4, ECAP-C/4, and FB-ECAP-A/4 conditions are reported in Figure 7.

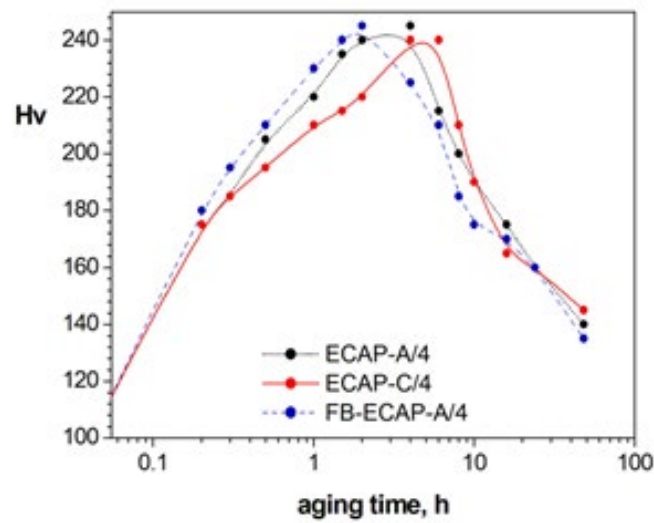


Fig.7 - Aging curves after ECAP-A/4, ECAP-C/4, and FB-ECAP-A/4 and subsequent aging at 540K for t ranging 10 min to 2 days (same times of the undeformed alloy T6-heat treatment).

Microstructure at hardness peak aging

Based on the aging curves of Figure 7, TEM inspections were carried out at the ECAP + aging hardness peak conditions. That is, the microstructures of the ECAP-A/4 + aging at 460K/3h, ECAP-C/4 + aging at 460K/5h, and FB-ECAP-A/4 + aging at 460K/2h were characterized in terms of the secondary-phase precipitation induced to grow (Figure 8).

Table 3 reports the meaningful statistics of the detected secondary-phase precipitates, and the mean cell and grain size.

The microstructure of the T8 hardness peak aged condition by all the three ECAP routes here analysed is characterized by the presence of both GP zones, secondary-phase precipitates at their early stage of formation and evolution, and some larger precipitate. The marked difference between the ECAP + aged at hardness peak (T8) and the undeformed T6 microstructures is represented by the presence of two more phases in the T8 condition. These are the Ω - $Al_x(CuLi)_y$ platelet-shaped phase lying at Al_{111} planes which are quite similar to T_1 precipitates, and S' - Al_2CuMg lath-shaped phase lying at Al_{210} planes showing a regular geometric planar morphology. The quantitative data reported in Table 3 show little differences of the number fraction of T_1 , θ' , and δ' phases.

On the other hand, as expected, little differences of the mean grain and cell size was found between the ECAP + aged at hardness peak, and ECAP + aged at 460K/6h condi-

tions. Moreover, the little microstructure differences among the different ECAP routes (A, C, and forward-backward route A) can be considered not significant.

To better understand the secondary-phase evolution induced during T6 and the two T8 (ECAP + aging) conditions, a cumulative histogram of all the four meaningful phases, that is, $(T_1 + \Omega)$, θ , δ , S , is reported in Figure 9. It appeared that T_1 phase tends to slightly reduce in favour of the S' phase as the aging time increases. The two other phases, θ' and δ' , did not seem to be influenced by the post-ECAP aging duration. In fact, they appeared not to change in number fraction from ECAP at 460K to ECAP at 460K followed by overaging at 460K/6h. Thus, ECAP shearing favoured the formation of S' , while it left unaltered the kinetics of the two other phases, θ' and δ' . The kinetic evolution of the most abundant T_1 phase was slightly affected by the shear strain-induced formation of the S' phase. Thence, S' phase only formed by the combined effect of tangled dislocations introduced by the pre-aging ECAP shear deformation, and this was not found to form upon T6-aging at 460K/6h.

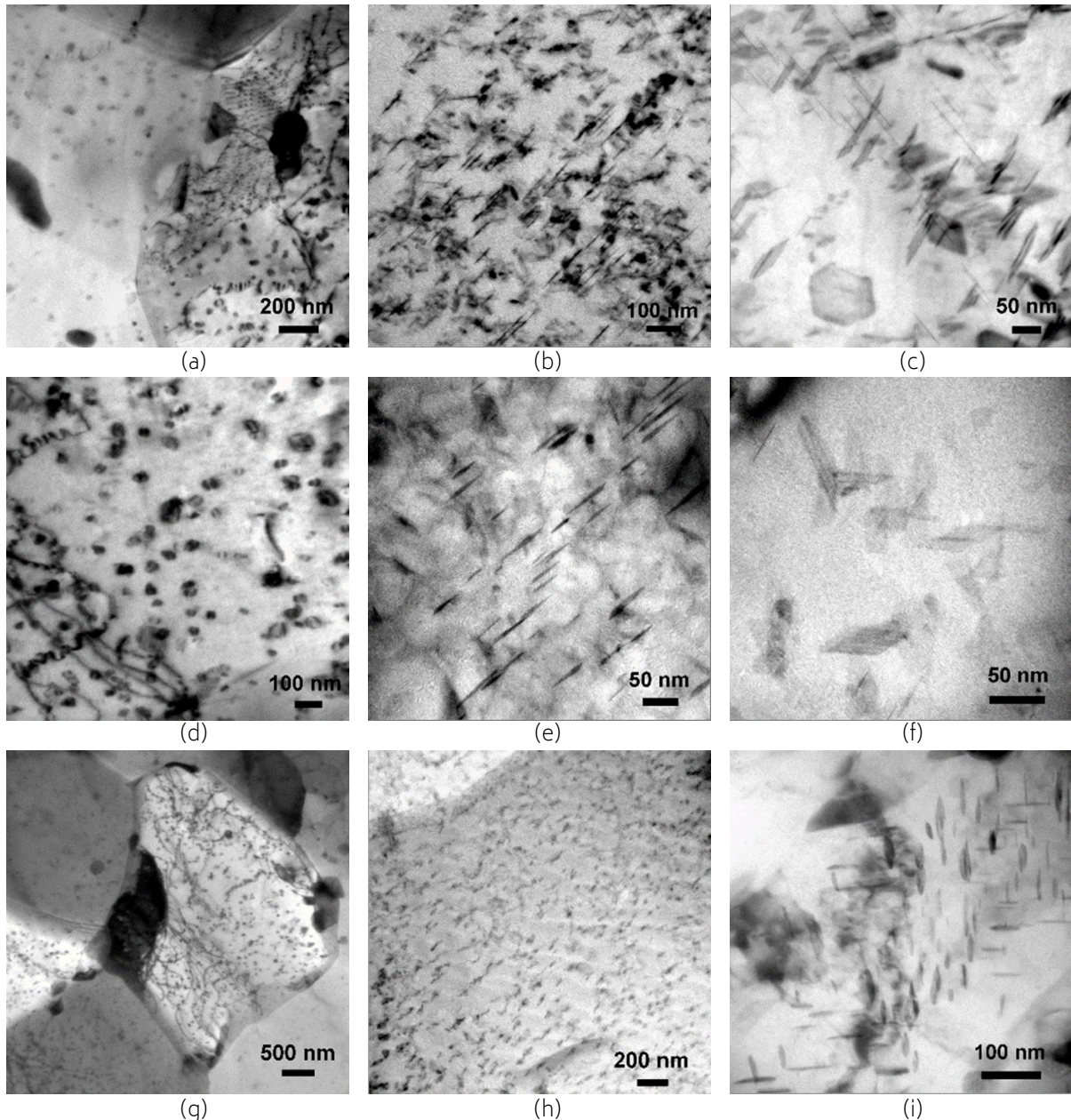


Fig.8 -Microstructures of the post-ECAP 460K aged alloys, with aging duration set at the maximum alloy hardness peak obtained after ECAP and subsequent aging at 460K: 3h for ECAP-A/4, 5 h for ECAP-C/4, 2 h for FB-ECAP-A/4. BF-TEM of ECAP-A/4 at Al_{002} , a), Al_{111} , b), and Al_{210} plane, c); ECAP-C/4 at Al_{002} , d), Al_{111} , e), and Al_{210} plane, f); FB-ECAP-A/4 at Al_{002} , g), Al_{111} , h), and Al_{210} plane, i).

The key microstructure feature that was here identified was the ECAP + aging-driven formation of a significant amount of S' phase and a small amount of Ω phase, which formed at the expense of a small amount of T_1 . Thence, these secondary-phase precipitation modifications induced by ECAP + aging involve a lithium redistribution. In fact, the T_1 phase is constituted by Al_2CuLi , while S' phase is Al_2CuMg . Thus, the induced formation of S' at the expense of a fraction of T_1 , was chemically accompanied by an equally stoichiometric sub-

stitution of Li with Mg. The Li now available in the Al-matrix is thermally favoured to form a further secondary-phase. This is chemically constituted by $Al + Cu + Li$, and most likely as $Al_x(CuLi)_y$, which is the Ω phase. Based on these findings and comparison with previously published results, the ECAP + aging precipitation sequence of the present $Al-3.0Cu-1.0Li-0.4Mg-0.4Ag-0.2Zr-0.5Sc$ alloy was: GP zones + $\beta - \theta'' + \theta' + \delta' + \beta + T_1 \rightarrow \beta + \theta + \delta + T_1 + (\Omega + S - T_1)$.

Tab.3 - Tangled dislocation density, ρ_{disl} , cell, D_{cell} and grain, D_g , size, secondary-phase precipitate mean number density, $n_V(T_1)$, $n_V(\Omega)$, $n_V(\theta)$, $n_V(\delta)$, $n_V(S)$, and size, d_{T_1} , d_{Ω} , d_{θ} , d_{δ} , d_S formed after ECAP-A/4, ECAP-C/4, and FB-ECAP-A/4 and subsequent aging at 460K to reach alloy hardness peak: 3h, for ECAP-A/4, 5 h, for ECAP-C/4, and 2 h, for FB-ECAP-A/4. Mean longer-edge lengths of the T_1 platelets, l_{T_1} , are also reported

	ECAP-A/4 +aged at 460K/6h	ECAP-C/4 +aged at 460K/6h	FB-ECAP-A/4 +aged at 460K/6h
$\rho_{disl} \cdot 10^{14} m^{-2}$	2.1 ± 0.5	1.0 ± 0.4	1.8 ± 0.4
D_{cell} , nm	300 ± 40	650 ± 50	220 ± 50
D_g , μm	1.5 ± 0.3	1.9 ± 0.3	1.6 ± 0.4
$n_V(T_1)$, μm^{-3}	190 ± 20	180 ± 15	180 ± 15
$n_V(\Omega)$, μm^{-3}	170 ± 15	160 ± 15	150 ± 15
$n_V(\theta)$, μm^{-3}	95 ± 5	90 ± 5	95 ± 5
$n_V(\delta)$, μm^{-3}	180 ± 5	190 ± 10	220 ± 20
$n_V(S)$, μm^{-3}	25 ± 5	20 ± 5	25 ± 5
d_{T_1} , nm	40 ± 4	45 ± 5	42 ± 4
d_{Ω} , nm	38 ± 4	40 ± 5	36 ± 4
d_{θ} , nm	30 ± 5	40 ± 5	25 ± 5
d_{δ} , nm	20 ± 5	25 ± 5	30 ± 5
d_S , nm	25 ± 5	20 ± 5	30 ± 5
l_{T_1} , nm	115 ± 10	145 ± 10	90 ± 10

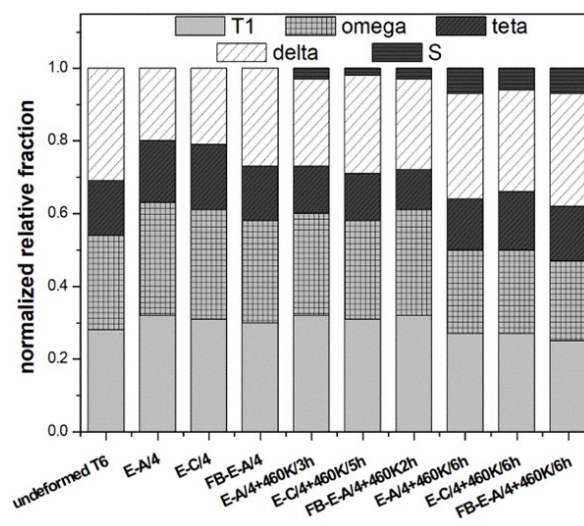


Fig.9 - Relative frequency of the strengthening secondary-phase precipitates in T6 undeformed alloy, after ECAP-A/4, ECAP-C/4, FB-ECAP-A/4 at 460K, after ECAP-A/4 + aging at 460K/3h, ECAP-C/4 + aging at 460K/5h, FB-ECAP-A/4 + aging at 460K/2h, and after ECAP-A/4, ECAP-C/4, FB-ECAP-A/4 + aging at 460K/6h. In the histogram, E stands for ECAP.

The statistical data calculated for the T_1 phase after ECAP + aging at hardness peak and after ECAP + T6 aging (where T6 aging refers to the hardness peak of the undeformed alloy) allowed a clear identification of a precipitate-coarsening rate. The data and linear interpolation are reported in Figure 10. The figure is a plot of the mean lateral size of the T_1 precipitates (platelet edge $l_{T_1+\Omega}$ aligned along the Al_{111} directions) vs. aging time, $t^{1/3}$ for the ECAP-A/4, ECAP-C/4, and FB-ECAP-A/4 followed by hardness peak aging and by alloy T6 aging. A linear interpolation was drawn with a sufficiently sound accuracy. This plot well indicates a power-law coarsening rate of the type: $l_{T_1+\Omega} = K_{LSW} \cdot t^{1/3}$. Here, $K_{LSW} = (8/9) \cdot (C_{solute} \cdot V^2 \gamma D_{inter} / RT)$, where C_{solute} is the phase solute concentration

of Cu and Li, V is the molar volume of both Cu and Li, γ is the phase/alloy interfacial energy, D_{inter} is the interdiffusion element coefficient (Cu, Li), R the Rayleigh constant, and T the temperature in Kelvin. This kind of power-law precipitate growth is in agreement with different previous models, such as the one very recently proposed by Jiang and co-workers [34]. This power-law phase growth was indeed first introduced by Lifshitz, Slyozov, Wagner, and thus named after them as LSW theory [35,36]. Moreover, a similar phase growth rate was also reported for δ [37], Al_3Sc [38], and θ [39] and other thermally activated phases in Al-Cu-X and Al-Cu-Li-X alloys [40].

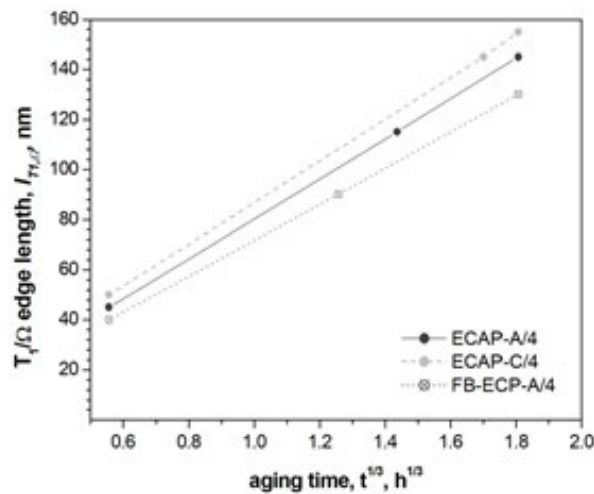


Fig.10 - $T_1+\Omega$ precipitate growth power-law. $T_1+\Omega$ plate/lath long-edge, $l_{T_1+\Omega}$, vs. $t^{1/3}$, where t is the aging time, for ECAP-A/4, ECAP-C/4, FB-ECAP-A/4 at peak aging.

CONCLUSIONS

The secondary-phase precipitation sequences of an Al-Cu-Mg-Li-Ag-Zr-Sc alloy subjected to different Equal-channel angular pressing (ECAP) routes (A, C, and forward-backward A) followed by aging was studied. The TEM inspections and the quantitative analyses of the existing phases allowed to identify the role of the ECAP shearing and post-ECAP aging on the relative fraction of the hardening phases. Thus, the following conclusions can be drawn.

- i). ECAP shearing and the introduced tangled dislocations were identified as responsible for a significant secondary-phase precipitation sequence acceleration. In particular, two phases were found to be greatly influenced by the presence of the tangled dislocations within the grained structure: the platelet T_1-Al_2CuLi , and the lath $S-Al_2CuMg$.
- ii). The ECAP + aging was responsible for lath-shaped $S-Al_2CuMg$ phase precipitation lying parallel to Al_{210} planes. This phase evolved and increased in number fraction with aging time at the expense of the T_1-Al_2CuLi and the platelet-shaped $\Omega-Al_x(CuLi)_y$ precipitate phases both lying at Al_{111} planes;
- iii). ECAP + aging induced the following precipitation sequence: GP zones + $\beta \rightarrow \theta'' + \theta' + \delta' + \beta + T_1 \rightarrow \beta + \theta + \delta + T_1 + (\Omega + S - T_1)$.
- iv). The $T_1+\Omega$ precipitates coarsening rate with aging time was found to be of Lifshitz-Slyozov-Wagner (LSW) type, that is as a power-law: $l_{T_1+\Omega} = K_{LSW} \cdot t^{1/3}$, $l_{T_1+\Omega}$ being the platelet and lath longer edge.

ACKNOWLEDGEMENTS

The EU-funded COST Action CA15102 - Solutions for Critical Raw Materials Under Extreme Conditions (CRM-EXTREME), website: <https://www.cost.eu/actions/CA15102>, is acknowledged for the material supply.

REFERENCES

- [1] T. Warner, Recently-developed aluminium solutions for aerospace applications, *Mat. Sci. Forum* 519-521 (2006) 1271-1278.
- [2] R.J. Rioja, J. Liu, The evolution of Al-Li base products for aerospace and space applications, *Metall. Mater. Trans.* 43A (2012) 3325-3337.
- [3] N. Eswara Prasad, A.A. Gokhale, R.J.H. Wanhill, *Aluminium-Lithium Alloys*, Elsevier, Oxford, 2014.
- [4] T. Dursun, C. Soutis, Recent developments in advanced aircraft aluminium alloys, *Mater. Des.* 56 (2014) 862-871.
- [5] E.J. Lavernia, T.S. Srivatsan, F.A. Mohamed, Strength, deformation, fracture behavior and ductility of aluminium-lithium alloys, *J. Mater. Sci.* 25 (1990) 1137-1158.
- [6] R.K. Gupta, N. Nayan, G. Nagasireesha, S.C. Sharma, Development and characterization of Al-Li alloys, *Mater. Sci. Eng. A* 420 (2006) 228-234.
- [7] R.K. Gupta, N. Nayan, G. Nagasireesha, S.C. Sharma, Development and characterization of Al-Li alloys, *Mater. Sci. Eng. A* 420 (2006) 228-234.
- [8] D. Ortiz, J. Brown, M. Abdelshehid, P. Deleon, R. Dalton, L. Mendez, J. Soltero, M. Pereira, M. Hahn, E. Lee, J. Ogren, R. Clark, J. Foyos, O.S. Es-Said, The effects of prolonged thermal exposure on the mechanical properties and fracture toughness of C458 aluminum-

- lithium alloy, Eng. Fail. Anal. 13 (2006) 170-180.
- [9] A. Deschamps, M. Garcia, J. Chevy, B. Davo, F. De Geuser, Influence of Mg and Li content on the microstructure evolution of AlCuLi alloys during long-term ageing, Acta Mater. 122 (2017) 32-46.
- [10] J.I. Perez-landazabal, M.L. No, G. Madariaga, V. Recarte, J. San Juan, Quantitative analysis of δ' precipitation kinetics in Al-Li alloys, Acta Mater. 48 (2000) 1283-1296.
- [11] B.C. Wei, C.Q. Chen, Z. Huang, Y.G. Zhang, Aging behavior of Li containing Al-Zn-Mg-Cu alloys, Mater. Sci. Eng. A 280 (2000) 161-167.
- [12] A.V. Mikhaylovskaya, A.G. Mochugovskiy, V.S. Levchenko, N. Yu. Tabachkova, W. Mufalo, V.K. Portnoy, Precipitation behavior of L12 Al₃Zr phase in Al-Mg-Zr alloy, Mater. Character. 139 (2018) 30-37.
- [13] Shuaishuai Qin, Seungwon Lee, Taiki Tsuchiya, Kenji Matsuda, Zenji Horita, Robert Kocisko, Tibor Kvackaj, Aging behavior of Al-Li-(Cu, Mg) alloys processed by different deformation methods, Mater. Design 196 (2020) 109139.
- [14] B. Decreus, A. Deschamps, F. De Geuser, P. Donnadieu, C. Sigli, M. Weyland, The influence of Cu/Li ratio on precipitation in Al-Cu-Li-x alloys, Acta Mater. 61 (2013) 2207-2218.
- [15] A.K. Khan, J.S. Robinson, Effect of silver on precipitation response of Al-Li-Cu-Mg alloys RID D-1730-2009, Mater. Sci. Technol. 24 (2008) 1369-1377.
- [16] M.J. Styles, R.K.W. Marceau, T.J. Bastow, H.E.A. Brand, M.A. Gibson, C.R. Hutchinson, The competition between metastable and equilibrium S (Al₂CuMg) phase during the decomposition of Al-Cu-Mg alloys, Acta Mater. 98 (2015) 64-80.
- [17] B.-P. Huang, Z.-Q. Zheng, Effects of Li Content on Precipitation in Al-Cu-(Li)-Mg-Ag-Zr Alloys, Scripta Mater. 38 (1998) 357-362.
- [18] I. Sabirov, M. Yu. Murashkin, R. Z. Valiev, Nanostructured aluminium alloys produced by severe plastic deformation: New horizons in development, Mater. Sci. Eng. A 560 (2013) 1-24.
- [19] A. Vinogradov, Y. Estrin, Analytical and numerical approaches to modelling severe plastic deformation, Progr. Mater. Sci. 95 (2018) 172-242.
- [20] M. Balog, F. Simancik, O. Bajana, G. Requena, ECAP vs. direct extrusion-Techniques for consolidation of ultra-fine Al particles, Mater. Sci. Eng. A 504 (2009) 1-7.
- [21] R.Z. Valiev, T.G. Langdon, Principles of equal-channel angular pressing as a processing tool for grain refinement, Progr. Mater. Sci. 51 (2006) 881-981.
- [22] M. Cabibbo, E. Evangelista, M. Vedani, Influence of Severe Plastic Deformations on Secondary Phase Precipitation in a 6082 Al-Mg-Si Alloy, Metall. Mater. Trans. 36A (2005) 1353-1364.
- [23] M. Cabibbo, Partial dissolution of strengthening particles induced by equal channel angular pressing in an Al-Li-Cu alloy, Mater. Character. 68 (2012) 7-13.
- [24] M. Cabibbo, A TEM Kikuchi pattern study of ECAP AA1200 via routes A, C, BC, Mater. Character. 61 (2010) 613-625.
- [25] M. Cabibbo, Microstructure strengthening mechanisms in different equal channel angular pressed aluminum alloys, Mater. Sci. Eng. A 560 (2013) 413-432.
- [26] H. Miyamoto, T. Ikeda, T. Uenoya, A. Vinogradov, S. Hashimoto, Reversible nature of shear bands in copper single crystals subjected to iterative shear of ECAP in forward and reverse directions, Mater. Sci. Eng. A 528 (2011) 2602-2609.
- [27] H. Alihosseini, M.A. Zaeem, K. Dehghani, A cyclic forward-backward extrusion process as a novel severe plastic deformation for production of ultrafine grains materials, Mater. Letters 68 (2012) 204-208.
- [28] H. Alihosseini, M.A. Zaeem, K. Dehghani, H.A. Shivaee, Producing ultrafine-grained aluminum rods by cyclic forward-backward extrusion: Study the microstructures and mechanical properties, Mater. Letters 74 (2012) 147-150.
- [29] M. Cabibbo, Shear induced low- and high-angle boundary characterization using Kikuchi bands in transmission electron microscopy, Mater. Sci. Forum 584-586 (2008) 293-298.
- [30] M. Cabibbo, W. Blum, E. Evangelista, M.E. Kassner, M.A. Meyers, Transmission electron microscopy study of strain induced low- and high-angle boundary development in equal-channel angular-pressed commercially pure aluminum, Metall. Mater. Trans. A 39 (2008) 181-189.
- [31] E.E. Underwood, Quantitative Stereology, Addison-Wesley Publishing Company, Reading, 1970.
- [32] T. Dorin, M. Ramajayam, S. Babaniaris, Lu. Jiang, T.J. Langan, Precipitation sequence in Al-Mg-Si-Sc-Zr alloys during isochronal aging, Materialia 8 (2019) 100437.
- [53] Gen Li, Naiqin Zhao, Tao Liu, Jiajun Li, Chunnian He, Chunsheng Shi, Enzuo Liu, Junwei Sha, Effect of Sc/Zr ratio on the microstructure and mechanical properties of new type of Al-Zn-Mg-Sc-Zr alloys, Mater. Sci. Eng. A 617 (2014) 219-227.
- [34] B. Jiang, F. Cao, H. Wang, D. Yi, Y. Jiang, B. Wang, H. Liu, F. Shen, Effect of aging time on the microstructure evolution and mechanical property in an Al-Cu-Li alloy sheet, Mater. Sci. Eng. A 740-741 (2019) 157-164.
- [35] I.M. Lifshitz, V.V. Slyozov, The kinetics of precipitation from supersaturated solid solutions, J. Phys. Chem. Solids 19 (1961) 35-50.
- [36] C. Wagner, Theorie der Alterung von Niederschlägen durch Umlösen (Ostwald Reifung), Z. Elektrochem. 65 (1961) 581-591.
- [37] B.A. Pletcher, K.G. Wang, M.E. Glicksman, Experimental, computational and theoretical studies of δ' phase coarsening in Al-Li alloys, Acta Mater 60 (2012) 5803-5817.
- [38] G.M. Novotny, A.J. Ardell, Precipitation of Al₃Sc in binary Al-Sc alloys, Mater. Sci. Eng. A 318 (2001) 144-154.
- [39] J. Murken, R. Höhner, B. Skrotzki, Strain path dependence of the precipitate size evolution of an Al-Mg-Li alloy under combined thermal and mechanical loading, Mater. Sci. Eng. A 363 (2003) 159-170.
- [40] C. Yang, D. Shao, P. Zhang, Y.H. Gao, J.Y. Zhang, J. Kuang, K. Wu, G. Liu, J. Sun, The influence of Sc solute partitioning on ductile fracture of Sc-microalloyed Al-Cu alloys, Mater. Sci. Eng. A 717 (2018) 113-123.